NANO · MICRO small
www.small-journal.com

# Bioinspired Hierarchical Porous Architecture for Enhanced Kinetics and Mechanical Integrity in Thick Cathode

*Ying Wang, Jihun Song, Luyao Huang, Leidong Xu, Hongyi Xu, Juner Zhu, and Hongli Zhu**

**Increasing the thickness of the electrodes is considered the primary strategy to elevate battery energy density. However, as the thickness increases, rate performance, cycling performance, and mechanical stability are affected due to the sluggish ion transfer kinetics and compromised structural integrity. Inspired by the natural hierarchical porous structure of trees, electrodes with bioinspired architecture are fabricated to address these challenges. Specifically, electrodes with aligned columns consist of tree-inspired vertical channels, and hierarchical pores are constructed by screen printing and ice-templating, imparting enhanced electrochemical and mechanical performance. Employing an aqueous-based binder, the $LiNi_{0.8}Mn_{0.1}Co_{0.1}O_2$ cathode achieves a high areal energy density of 15.1 mWh cm$^{-2}$ at a rate of 1C at mass loading of 26.0 mg cm$^{-2}$, benefitting from the multiscale pores that elevated charge transfer kinetics in the thick electrode. The electrodes demonstrate capacity retention of 90% at the 100th cycle at a high current density of 5.2 mA cm$^{-2}$. To understand the mechanisms that promote electrode performance, simplified electro-chemo-mechanical models are developed, the drying process and the charge-discharge process are simulated. The simulation results suggested that the improved performance of the designed electrode benefits from the lower ohmic overpotential and less strain gradient and stress concentration due to the hierarchical porous architecture.**

## 1. Introduction

The growing demand for high energy density in commercial lithium-ion batteries (LIBs) used in electronic devices and vehicles highlights the significance of thick electrodes.[1,2] Increasing electrode thickness efficiently boosts the active material proportion of the entire LIB, thereby contributing to energy density improvement. However, the presence of thick electrodes lengthens the transport distance for ions to the current collector and electrons to the separator direction, thereby reducing the efficiency of ionic and electronic transfer and active materials utilization.[3] At high rates, limited ion transfer kinetics is identified as the primary reason for the insufficient capacity of the LIBs electrode.[4] Therefore, creating ample space for electrolyte penetration and shortening ionic transfer distance to reduce ion tortuosity and maximize ion transfer kinetics are effective strategies for enhancing the rate performance of thick electrodes.[5] Besides the kinetics concerns, the fragile mechanical performance of thick electrodes requires further advancements to enhance structural integrity and a satisfactory lifespan for these electrodes.[6,7] During electrode drying, capillary pressure fosters the formation of numerous uneven cracks, negatively impacting both the mechanical and electrochemical stability of the electrodes.[8] Additionally, the cracking issue worsens as the electrode thickness increases due to strong sedimentation and weak diffusion of the coating.[9]

To address the aforementioned challenges, we sought inspiration from nature. Trees have numerous longitudinally arranged microchannels that, in conjunction with their uniquely hierarchically structured porous network, enable water delivery through capillary action based on the cohesion-tension theory of transpiration.[10] In electrochemical applications, the inherent low-tortuosity structure of tree-derived wood was utilized as a template to boost the ionic transfer kinetics during cycling and improve the capacity of electrodes at high current rates.[11] Additionally, a reasonable spacing between trees allows them to release internal pressure without exerting pressure on neighboring trees. Roots have the potential to bolster the stability of the tree in the soil, allowing it to tolerate heightened pressure and maintain the towering stature of trees.[12] Implementing this structure in electrodes mitigates the stress caused by volume change during electrode processing and battery cycling, improves the connection between the electrode and the current collector, and ensures the structure integrity of electrodes. Based on these hypotheses, it is imperative to effectively produce electrodes with tree-inspired structures.

Screen printing is an attractive approach for producing thick 3D electrodes with a precisely designable and controllable

Y. Wang, J. Song, L. Huang, J. Zhu, H. Zhu
Department of Mechanical and Industrial Engineering
Northeastern University
Boston, MA 02115, USA
E-mail: h.zhu@neu.edu
L. Xu, H. Xu
School of Mechanical, Aerospace, and Manufacturing Engineering
University of Connecticut
Storrs, CT 06269, USA

The ORCID identification number(s) for the author(s) of this article can be found under https://doi.org/10.1002/smll.202406058

**DOI: 10.1002/smll.202406058**

 

tree-inspired structure without material waste.[13,14] Unlike subtractive methods such as etching or machining, which involve removing materials to achieve the desired shape, screen printing is an additive manufacturing that does not generate any material waste during fabrication. Despite its advantages, the resolution of printed electrodes is limited to ≈ 50 µm due to technological constraints. Therefore, an additional approach is necessary to create smaller vertical microchannels in tree-inspired electrodes and achieve efficient ion transfer. Among viable approaches for fabricating narrow vertical channels, ice-templating is a promising candidate that does not require specific materials (unlike techniques that rely on sacrificial phases),[15–18] and does not involve the introduction of excessive carbon (a drawback associated with carbon-based templating methods).[11,19–22] or excessive binder (a limitation of the phase inversion method).[23] The fabricated electrodes exhibit distinct hierarchical pores, consisting of microchannels formed by ice-templating and microscopic pores created through solvent evaporation. Compared to integrating with other methods, such as spinning, spraying, filtration, gelation, and 3D printing, to fabricate low tortuosity electrodes, screen printing in the presence of highly structurally controllable and can realize continuous and scalable industrialization.[24]

Inspired by natural trees, we are the first to construct tree-inspired electrodes with hierarchical porous architecture to boost the ion transfer kinetics and enhance the structural stability of single crystalline $LiNi_{0.8}Mn_{0.1}Co_{0.1}O_2$ (NMC 811) thick electrodes. Screen printing and ice-templating techniques were employed to provide electrodes with the tree-inspired structure. Notably, the aqueous-based NMC 811 electrode slurry was used in the whole process for two reasons. First, there is a desire to replace toxic and expensive NMP as a solvent with environmentally friendly and inexpensive water to reduce the cost of NMC electrode manufacturing and minimize environmental pollution. Second, based on the design of the equipment and the principle of this technique, ice-templating is currently only applicable to the use of water as a solvent. A unique cellulose binder was applied to protect the NMC 811 particles from proton exchange during the aqueous processing, thus maintaining the structure integrity of NMC 811 particles and ensuring reasonable electrode capacity.[25] Compared to electrodes dried at ambient temperature, the tree-inspired electrodes with hierarchical pores demonstrate enhanced rate performance and cycling stability. Furthermore, we conducted in-depth modeling to visualize the improvement in the electrochemical and mechanical characteristics of the tree-inspired structure. The extensively tailorable electrodes can be utilized to accurately and thoroughly understand the correlation between their structure, electrochemical performance, and mechanical behavior. Moreover, given the large-scale manufacturing capabilities of both technologies, the proposed tree-inspired electrodes have substantial potential for industrial adoption.

## 2. Results and Discussion

The design of high-performance electrodes for energy storage devices can draw inspiration from nature's efficient structures. This study explores the parallels between natural trees and tree-inspired electrodes with multiscale porosity, as illustrated in **Figure** 1A. In nature, trees possess microchannels with distinct hierarchical pores that facilitate the efficient transport of water and nutrients. Additionally, space between trees allows them to grow without disturbance from neighbors, and tree roots firmly anchor them in the soil, ensuring upright growth. The electrode microchannels, formed by ice-templating and solvent evaporation, contain tiny pores that create well-defined hierarchical pores, maximizing ion transfer kinetics. Additionally, the screen-printed pattern provides space for electrode components to release internal stress during drying and acts as an effective "root" to enhance the connection between the electrode and the current collector. These biomimetic structures enable tree-inspired electrodes to outperform conventional electrodes in both electrochemical and mechanical properties. Figure 1B illustrates the effect of electrode structure on ionic transfer kinetics, while Figure 1C demonstrates the enhanced mechanical stability of tree-inspired electrodes compared to conventional ones.

Screen printing and ice-templating are used to construct the multiscale pores and create tree-inspired electrodes. **Figure** 2A shows and summarizes the fabrication methods and microstructures of the tree-inspired electrodes. The *first-level pores* of the electrodes are fabricated using screen printing. Adequate column spacing alleviates internal stress during the drying process and ensures structural integrity, while the first-level pores facilitate ions diffusion and electrolyte wetting, enhancing electrochemical kinetics. After the electrode materials were patterned and transferred to the current collector, the current collector was placed on a copper plate immersed in liquid nitrogen. Upon contact between the current collector and the copper plate, ice pillars formed vertically due to the rapid heat transfer capabilities of the metal. After freeze-drying, the areas where icicles were located constructed narrow vertical channels. These are the *second-level pores*, which shorten the ion transfer pathway and enhance ion transfer kinetics in the electrodes. Concurrently, *third-level pores* were produced due to solvent evaporation, providing room for electrolyte storage and ion diffusion.

The geometric dimensions of these three levels of pores are highly controllable. The first-level pores are determined by the printing pattern. The second-level pores are majorly influenced by freezing directions and cooling rates. Meanwhile, the dimensions of the third-level pores are greatly affected by the solid content of the slurry. Slurries with higher solid content result in lower electrode porosity after the ice-templating (Figure S1, Supporting Information). A highly porous structure enhances the ion transfer kinetics of electrodes, but high porosity reduces electrode energy density. Additionally, increased use of solvents and subsequent higher energy consumption during the drying procedure lead to higher manufacturing costs. However, without altering the formulation, aggressively increasing the solid content of the slurry negatively impacts the component distribution and viscosity of the electrode slurry, reducing the uniformity and integrity of the coating and thereby impairing the electrochemical and mechanical properties of the electrodes. Based on the materials, formulation, viscosity, and particle dispersion situation of the slurry in this work, a slurry with 50% solid content was prepared and applied in the following fabrication and evaluation.

Comprehensive analysis and characterization of the structural design of the electrode are crucial for revealing the relationship between the architecture and electrochemical properties of electrodes. The electrode morphology was characterized through

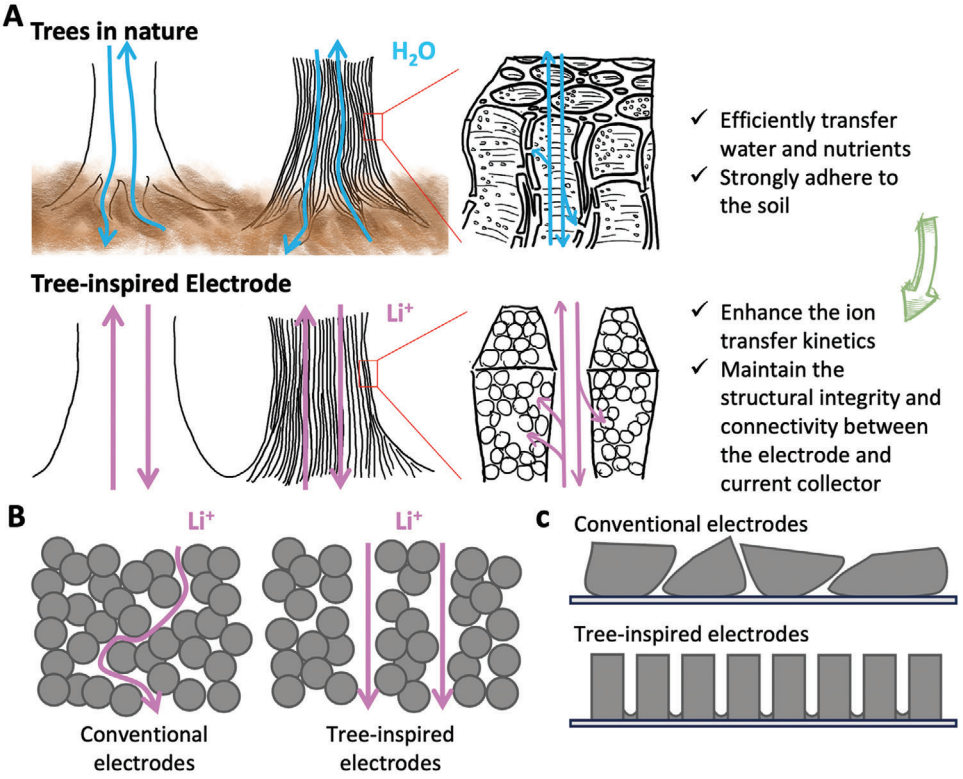


**Figure 1.** Schematic illustration of A) natural trees and the tree-inspired electrode with multiscale pores, B) lithium ions transfer paths, and C) structural integrity of conventional and tree-inspired electrodes.

scanning electron microscopy (SEM). Figure 2B illustrates the overall structure of the tree-inspired electrode. The columnar electrodes are arranged in a staggered pattern. Each electrode column has a diameter of 500 μm, with a spacing of 250 μm between neighboring electrodes. The configuration aligns with the stencil (Figure S2, Supporting Information). Using optimal electrode slurry and appropriate operation ensures the integrity and stable formation of the printed vertical columns. Figure 2C demonstrates that the printed columns can reach a maximum height of ≈ 700 μm in a single printing layer. Within each column, numerous vertical microchannels are created by ice-templating. Figure 2D illustrates a top-view SEM image of the long strips of second-level pores. Figure 2E shows a cross-sectional view of the electrode, aligned parallel to the side with ice growth. Specifically, the microstructure of the ice-templated electrode is organized in a vertical laminated pattern that is the same as the ice structures. Figure 2F displays the cross-sectional view of the surface of the laminated structural electrode, observed from a direction perpendicular to the icicle formation. It reveals the presence of definite third-level pores lacking any second-level pores. The higher solid content in slurry results in tinier icicle creation with narrower vertical channels and thicker wall formation. In this case, the constructed channels are ≈ 10 μm wide with walls ≈ 23 μm thick. The particles predominantly occupy the majority of the electrode volume, mitigating the adverse effects of the highly porous structure on the energy density of electrodes.

For the purpose of revealing the relationship between electrode structure and electrochemical performance, four types of electrodes with various structures are labeled according to their production process: normal-dried-bar coated (BC), normal-dried-screen printed (SP), ice-templated-BC, and ice-templated-SP. The fabrication details and corresponding structures of each type of electrode are provided in Table S2 (Supporting Information). Among these, the ice-templated-SP electrode exhibits a tree-inspired structure featuring all three levels of pores.

Rate performance tests were conducted using constant current-constant voltage (CC-CV) charging at C/3 and constant current (CC) discharging at various rates of 0.1, 0.5, 1, 2, 3, 4, and 6C to elucidate the relationship among electrochemical performance, kinetics, and multiscale pores. The 1C equals to 200 mAh $g^{-1}$. The electrochemical performances of ice-templated-BC and normal-dried-BC electrodes were compared at a mass loading of 15.4 mg $cm^{-2}$. **Figure** 3A shows that the normal-dried electrodes have a higher discharge capacity than the ice-templated sample at low rates of 0.1 and 0.5C. The low-rate capacity is primarily determined by the limited connection between carbon particles in the extremely porous electrodes. The capacity relationship between these two electrodes is inverted at the current rate of 1C. The advantages of the second-level pores in terms of capacity are revealed when the primary chemical reaction is mainly influenced by the ionic conductivity. At 3C, the ice-templated-BC electrode delivers a much higher discharge capacity of 98 mAh $g^{-1}$, approximately twice that of the normal-dried-BC electrode (53 mAh $g^{-1}$). Figures 3B,C plot the charge-discharge curves of the ice-templated-BC and normal-dried-BC electrodes, respectively. The constant voltage (CV) step has minimal impact on capacity, while

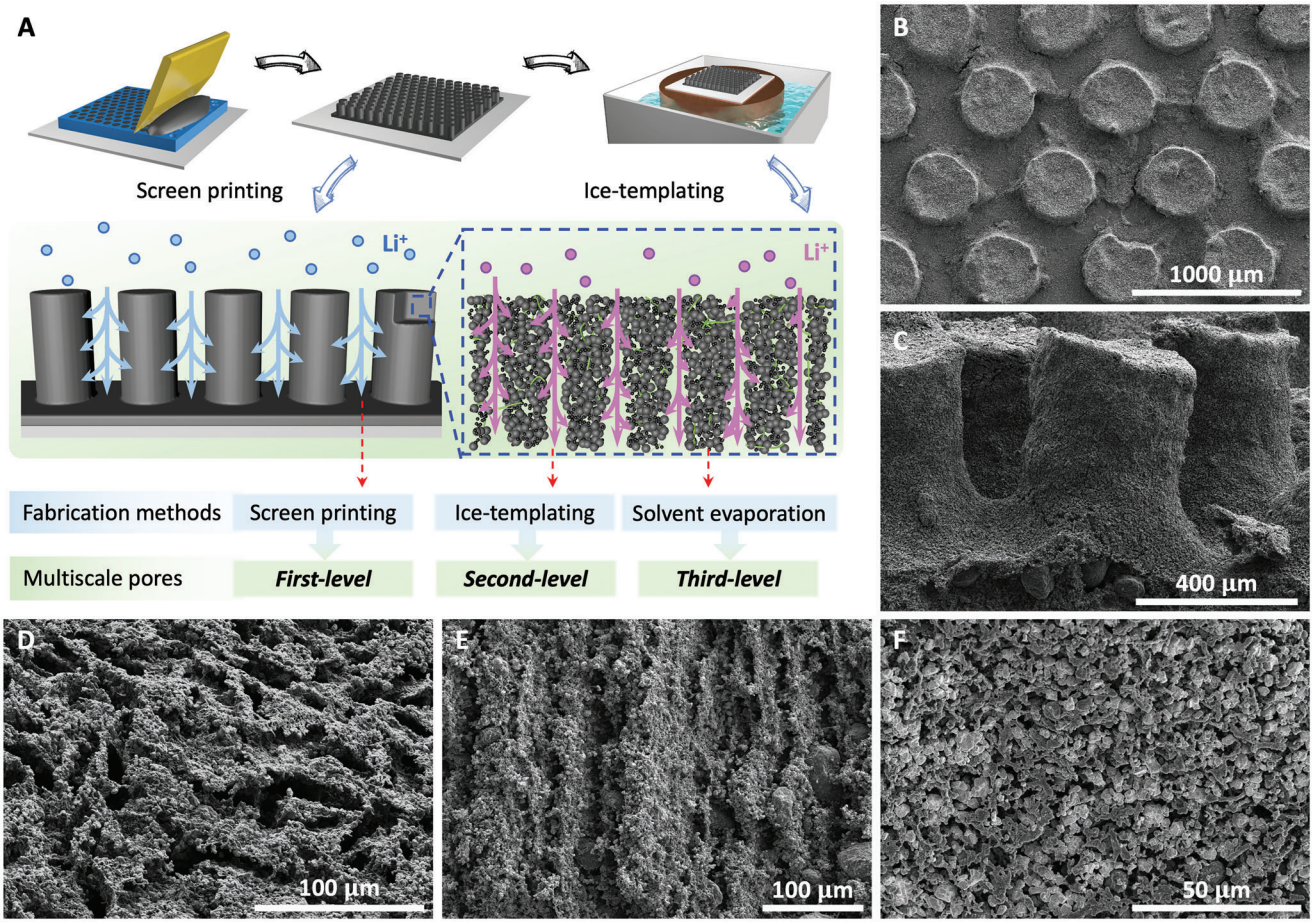


**Figure 2.** Schematic of the fabrication process and SEM images of low tortuosity tree-inspired electrodes with multiscale pores. A) Electrodes with multiscale porosity fabricated by screen printing, ice-templating, and solvent evaporation. B) Top view and C) cross-sectional SEM image of as-printed patterns with the first-level pores. Section of electrode columns from D) top view and cross-sectional view at E) parallel and F) perpendicular to the icing direction.

the overall charge capacity largely depends on the potential gaps and capacity provided during the CC step. At 2C, the potential gap of the ice-templated-BC electrode is 1.35 V at a capacity of 80 mAh $g^{-1}$, and the CC process renders a large capacity of 125 mAh $g^{-1}$. Meanwhile, the normal-dried-BC electrode displays a potential gap of 1.97 V at the same capacity, and the CC process provides a capacity of 102 mAh $g^{-1}$.

Thicker electrodes with a mass loading of 26.0 mg $cm^{-2}$ were prepared to evaluate the advantage of multiscale pores for fast-charging applications. Figure 3D compares the discharge capacities of ice-templated-BC and ice-templated-SP electrodes at various current rates. Both electrodes show comparable discharge capacity at low rates of 0.1C and 0.5C. However, the capacity of the ice-templated-SP electrode indicates the effectiveness of its multiscale pores at a current rate of 1C, and the capacity difference becomes even more pronounced as the rate increases from 1 to 4C. At 3C, the ice-templated-SP electrode delivers a discharge capacity of 97 mAh $g^{-1}$. Also, it provides a high areal energy density of 15.1 mWh $cm^{-2}$ at a current density of 1C, which is almost seven times higher than that of the ice-templated-BC electrode. The charge-discharge curves of the two electrodes are plotted in Figures 3E,F. It can be observed that the ice-templated-BC electrode exhibits a significant decrease in capacity from 0.5C to 3C. It follows that at high current rates equal to or above 3C, the charge capacity of the ice-templated-BC electrode is predominantly generated by the CV step. In contrast, the ice-templated-SP electrode achieves a charge capacity of 82 mAh $g^{-1}$ in the CC process and a total of 97 mAh $g^{-1}$ at a rate of 3C, corresponding to an areal energy density of 7.7 and 9.1 mAh $cm^{-2}$, respectively. Compared to other thick NMC electrodes, Figure S3 and Table S1 (Supporting Information) demonstrate that the ice-templated-SP electrodes have improved electrochemical properties due to the presence of hierarchical pores.

Physics-based models based on real microstructures have turned out to be a useful technique for fundamental insights into electrode design. However, the highly hierarchical porous structure posed the modeling computational challenges because the pores cover 2–3 orders of magnitude in length scale. The computational efficiency is further challenged by the multiphysical nature of the problem. Therefore, in this paper, we adopted simplified models to capture the main physical processes. A microstructure-resolved model was developed to cover the second and third levels of the pores. The microstructure of the active materials and the pores were created by reconstructing SEM

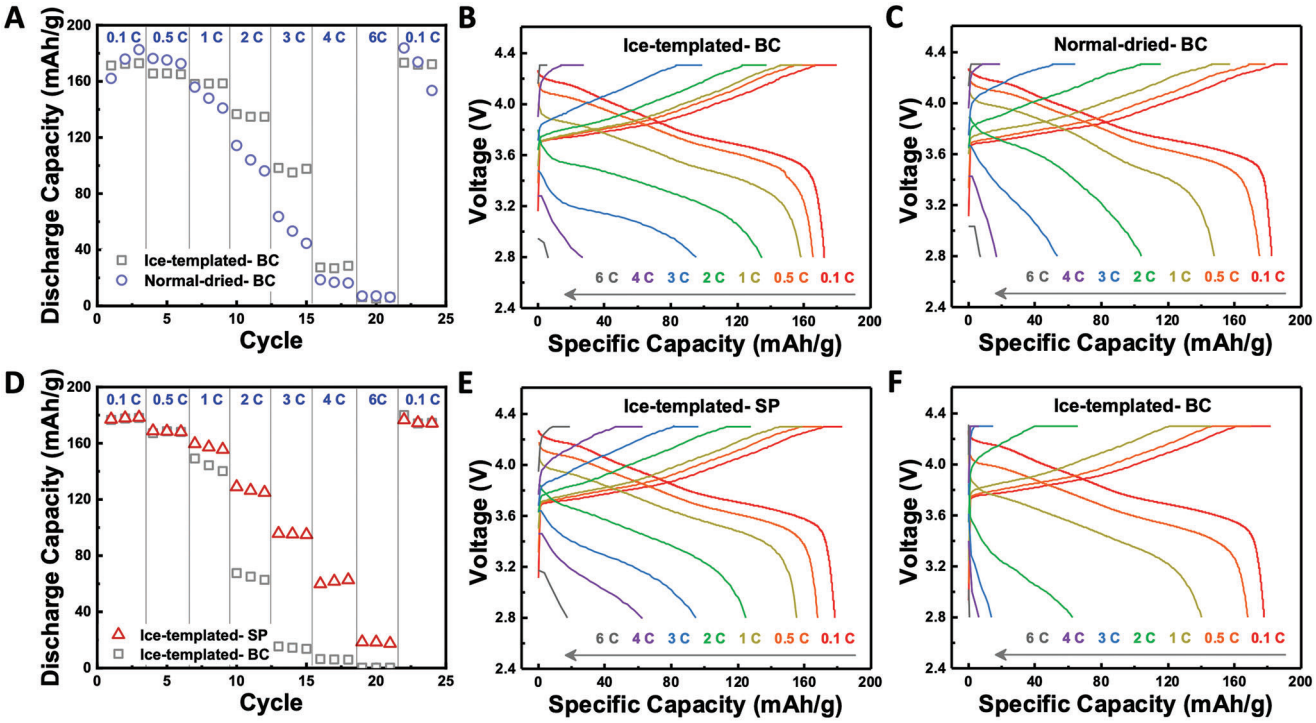


**Figure 3.** Electrochemical performances of electrodes fabricated by various technologies. All electrodes were operated with a CC-CV charge and CC discharge process. A) Rate performance of the ice-templated-BC and normal-dried-BC electrodes. Charge-discharge curves of the B) ice-templated-BC and C) normal-dried-BC electrodes. The mass loading is 15.4 mg $cm^{-2}$. D) Rate performance of the ice-templated-SP and ice-templated-BC electrodes. Charge-discharge curves of the E) ice-templated-SP and F) ice-templated-BC electrodes. The mass loading is 26.0 mg $cm^{-2}$. Li metal is 110 µm in thickness for all cells. All electrodes were charged using CC-CV at C/3 and discharged at various rates.

images as shown in Figures S4A,B (Supporting Information), and the electrolyte was set to fill the pores. The domain, boundary, and governing equations to the active material and electrolyte are applied to the microstructure as shown in Figure S4C (Supporting Information). The parameters used in this model are collected from literature[26] and are described in Table S3 (Supporting Information). We used the model to simulate the charging process at 4C and calculated the voltage profile (**Figure** 4A) and average von Mises stress (Figure 4B). Ice-templated-BC sample shows lower voltage at the initial state which is related to activation overpotentials and an ohmic overpotential than the normal-dried-BC sample. Since we used the same material for the ice-templated-BC sample and normal-dried-BC sample, the activation overpotential is the same. Therefore, the difference in the initial voltage can be attributed to the ohmic overpotential. The increased reaction surface area (interface between the electrolyte and the active materials) by the second-level pores decreases the ohmic overpotential, leading to 18% higher capacity at 4C. Although the simulated structure is only a small portion of the whole electrode, it serves as a representative volume element (RVE) and the simulation results agree well with the experimental observations.

The ice-templated-BC sample also shows improved mechanical stability. Less stress concentration and gradient of strains are observed. In the charge-discharge process, the diffusion-induced strain (or eigenstrain) depends on the lithium concentration. Based on the linear elasticity constitutive law, stress concentration occurs when the gradient of lithium concentration becomes large inside the electrode. An interesting finding is that the ice-templated-BC samples experience more strain at the end of charging than the normal-dried-BC samples because of a deeper charge, but the stress in the ice-templated-BC samples is still lower in all charging processes. This interesting finding highlights the importance of the hierarchical structure of the electrode, resulting in a slower accumulates of stress. Furthermore, we performed 3D analysis while charging for 50% (450 s) for both normal-dried-BC and ice-templated-BC which have the same average concentration (Figure 4C–6J). In normal-dried-BC, a large lithium concentration gradient occurred in both the active material and electrolyte (Figure 4C–E), and this lithium concentration gradient induces high overpotential and high stress.[27] On the other hand, in ice-templated-BC, a relatively low concentration gradient of lithium ions occurred in both the active material and electrolyte (Figures 4D–F). Therefore, normal-dried-BC showed higher overpotential and higher stress than ice-templated-BC (Figure 4G–J).

Although ice-templating provides the second- and third-level pores to enhance the electrochemical kinetics of electrodes, the electrodes are brittle and have poor mechanical properties. An appropriate structural design can minimize internal stresses that arise during the drying process and long-term cycling, therefore reducing crack formation and maintaining the structural integrity of electrodes. **Figure** 5A displays electrode cracks created by internal stresses. The normal-dried-BC electrode exhibits noticeable cracks and delamination of electrodes from the current collector. In contrast, the normal-dried-SP electrode shows no

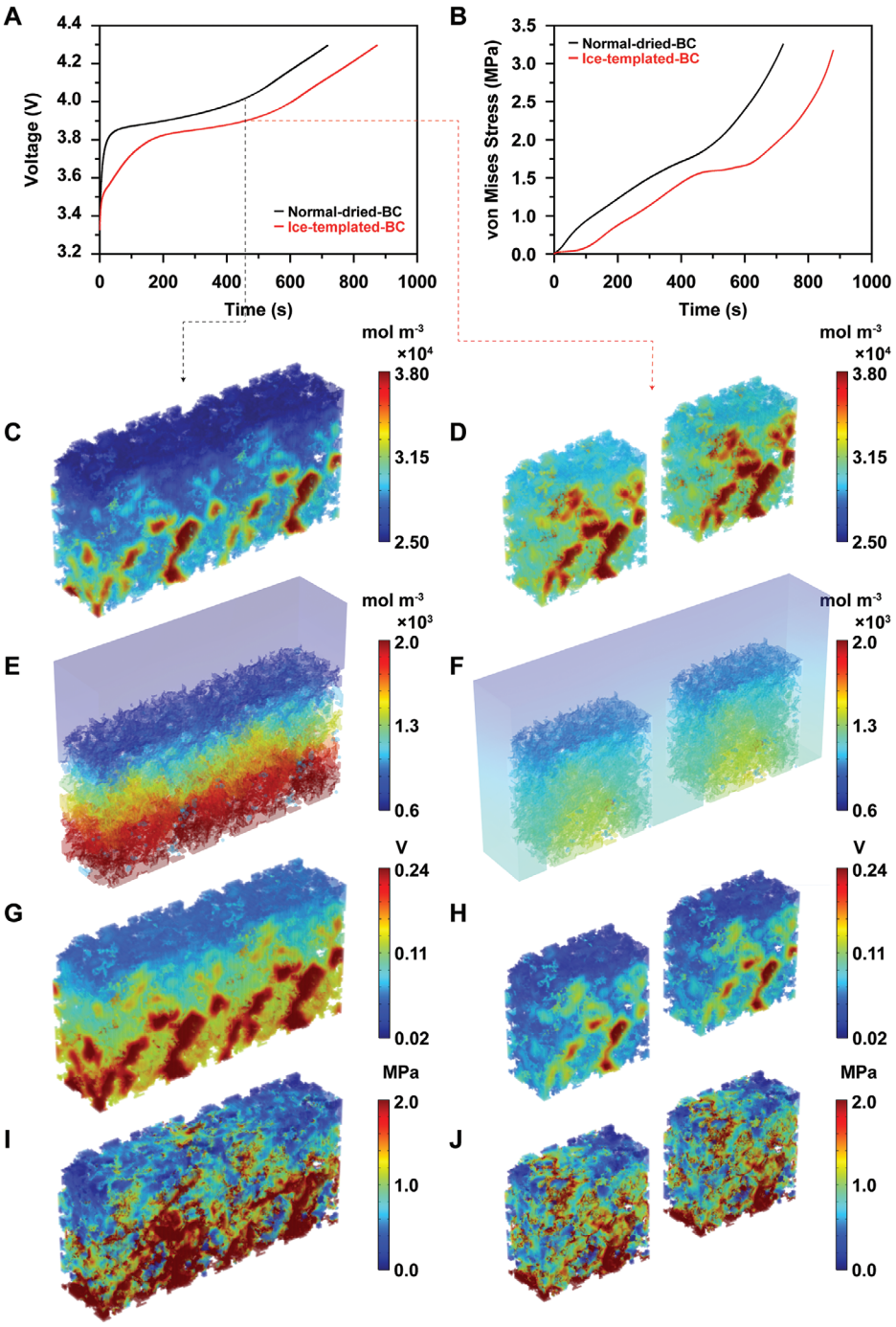


**Figure 4.** Electro-chemo-mechanical modeling for second- and third-level pores generated in normal-dried-BC and ice-templated-BC samples. A) Voltage profiles, B) average von Mises stress profiles, and 3D analysis at 50% charging (450 s): lithium concentration in active materials in C) normal-dried-BC sample and D) ice-templated-BC sample, lithium concentration in electrolyte in E) normal-dried-BC sample and F) ice-templated-BC sample, overpotential in G) normal-dried-BC sample and H) ice-templated-BC sample, and von Mises stress in I) normal-dried-BC sample and J) ice-templated-BC sample.

obvious disruptive cracks, suggesting the mechanical stability advantages conferred by the first-level pores. This advantage is also observed for the ice-templated electrodes.

Figure 5B illustrates the typical procedure of penetrating cracks formation in the conventional electrodes during the drying procedure. 1) The undulating liquid surface arises between particles and the solution; 2) Ripples with the sharpest curves generate the highest capillary pressure and internal stress; 3) Cracks form to relieve this internal stress, and as the drying process intensifies, the unexpected cracks run through the entire electrode.

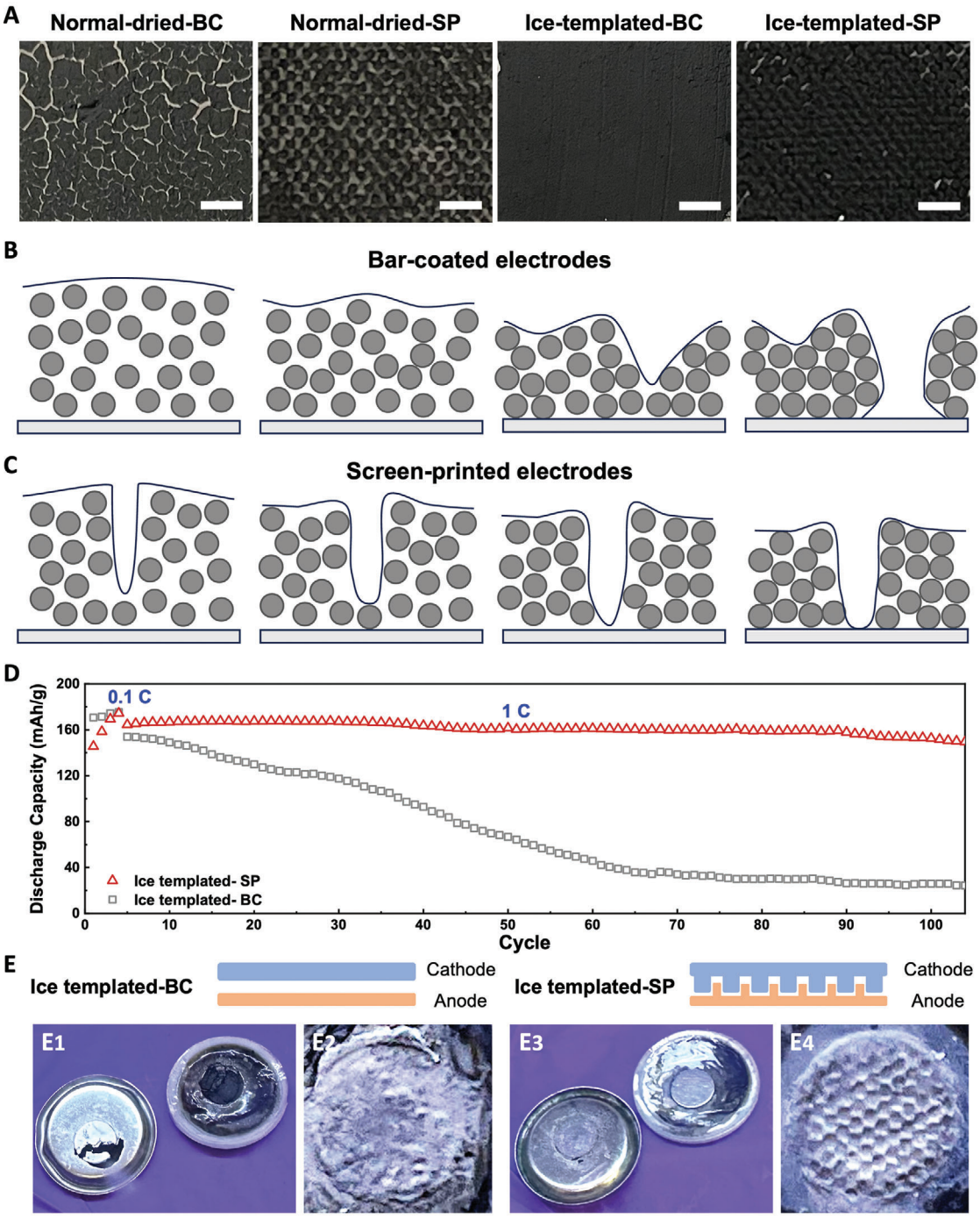


**Figure 5.** The structural integrity of electrodes fabricated and dried by various methods. A) Digital images of thick normal-dried-BC, normal-dried-SP, ice-templated-BC, and ice-templated-SP electrodes. The scale bar is 0.2 cm in all figures. Schematics of B) conventional and C) tree-inspired electrodes during the drying process. D) Cycling stability of the ice-templated-SP and ice-templated-BC electrodes. E) Digital images of NMC 811 cathode and Li metal anode after long-term cycling. All electrodes were charged using CC-CV at C/3 and discharged using CC at 1C. The mass loading is 26.0 mg $cm^{-2}$ and Li metal is 110 µm in thickness for all cells.

Meanwhile, excessive localized forces pull on the bottom particles, resulting in delamination from the current collector. Conversely, the tailored first-level pores effectively reduce the occurrence of these unexpected cracks, as shown in Figure 5C. Since the capillary forces resulting from the interfacial curvature are significantly weaker than those from preexisting cracks, the latter primarily relieve internal tension throughout the drying process. Simultaneously, the particles move horizontally from the original crack location to the bulk electrode, and no unexpected delamination occurs between the electrode and the current collector.

Slowing down the drying rate of the electrodes reduces significant fluctuations in internal stresses that occur during the drying process. As a result, it becomes difficult to visually differentiate the structural integrity of ice-templated electrodes with bare eyes (Figure 5A). In this context, the effects of first-level pores on the structural stability of ice-templated electrodes were revealed through long-term cycling performance evaluation. The cycling stability of electrodes is significantly influenced by their mechanical integrity, as discontinuous connections between electrode components and delamination between electrodes and the current collector disrupt electron transfer pathways. In severe cases, extensive detachment of electrodes or materials improperly penetrated across the separator can result in permanent capacity loss or potential safety risks. The preceding digital images clearly show the substandard mechanical properties of normal-dried-BC electrodes, leading to significantly inferior cycle stability compared to ice-templated-BC electrodes (Figure S5, Supporting Information). Meanwhile, short circuits were observed for some normal-dried-BC electrode samples during the long-term cycling (Figure S6, Supporting Information).

The benefits of first-level pores in the long-term cycling performance of the ice-templated electrodes are discussed below. Figure 5D depicts the cycling stability of these two Ice-templated electrodes at a current rate of 1C, which equals the current density of 5.2 mA $cm^{-2}$. The ice-templated-BC electrode displays significant capacity decay in the initial cycling stages, resulting in a capacity of 24 mAh $g^{-1}$ after 100 cycles, corresponding to a capacity retention of 16%. While compared to the ice-templated-BC electrode, the ice-templated-SP electrode demonstrates a significantly superior capacity of 150 mAh $g^{-1}$ after 100 cycles, equivalent to 90% of its initial capacity. This high capacity retention is exceptional among current thick NMC electrodes at high current densities (Figure S7, Supporting Information).

In order to gain a deeper comprehension of the factors contributing to the exceptional cycle durability of ice-templated-SP electrodes, the batteries were dismantled subsequent to the cycling test. Figure 5E displays the digital images of the NMC 811 cathode and Li metal anode after cycling. After cycling, Figure 5E1 shows that part of the electrode is affixed to the separator, while another portion remains on the battery case with the current collector. This partial delamination of the ice-templated-BC electrode and current collector indicates poor connectivity between them and weak structure integrity of electrodes. Furthermore, the Li metal surface of the ice-templated-BC half-cell displays irregular clusters (Figure 5E2), suggesting uneven Li deposition during cycling. In contrast, the ice-templated-SP electrode and current collector remain intact and firmly attached to the separator (Figure 5E3). The printed structure not only relieves internal stress and ensures structural integrity but also patterns the soft Li metal (Figure 5E4). Patterned Li metal has advantages in achieving mechanical interlocking with the ice-templated-SP electrode, boosting the connection between the cathode and Li metal and reducing the overall distance for ion transfer. Moreover, either aggregation or dendrite is observed on the patterned Li metal, suggesting a beneficial effect during the Li plating and extending cycle performance. Similar conclusions have been reported in the previous study.[28]

To understand the stress distribution during the drying process, we reconstructed the microstructures based on SEM images (**Figures** 6A,B) of the ice-templated-BC samples and ice-templated-SP samples and developed models using the hygroscopic swelling theory based on 17453 and 16967 elements, respectively (Figure 6C). The models were simulated until the water concentration reached zero, assuming constant and complete drying over 24 h. The parameters are summarized in Table S4 (Supporting Information), and the equations are described in the Experimental section. The enlarged surface area in the ice-templated-SP sample reduced the drying time by 47.46% compared to the ice-templated-BC sample ((Figure 6D). On the other hand, the fully dried ice-templated-SP sample showed only 39.02% of the stress occurred in the fully dried ice-templated-BC sample in magnitude (Figure 6E). It was also found that the ice-templated-BC sample showed concentrated stress in the center of the structure (Figure 6F), while the ice-templated-SP sample showed uniform stress overall (Figure 6G).

## 3. Conclusions

Inspired by the structure of trees, we utilized screen printing and ice-templating techniques to fabricate tree-inspired thick electrodes. Similar to the natural design of trees, these electrodes feature columnar arrangements with numerous vertical microchannels and hierarchical pores architecture. The multiscale pores maximize ion transfer kinetics and enhance the capacity of electrodes at high rates. At a high rate of 3C, the tree-inspired thick electrode with 26.0 mg $cm^{-2}$ mass loading delivers a high discharge capacity of 97 mAh $g^{-1}$. The high massloading electrode delivers an areal energy density of 15.1 mWh $cm^{-2}$ at the rate of 1C. Simultaneously, the tree-inspired structure reduces the internal stresses of the thick electrode and enables it to remain structurally intact without any apparent cracks, contributing to a high capacity retention of 90% at the 100th cycle under a high current density of 5.2 mA $cm^{-2}$. Furthermore, the improvement in mechanical characteristics of the screen-printed structure (the first-level pores) was studied through the development of a drying process model. As a result, ice-templated-SP showed better characteristics not only in terms of drying time (24% faster) but also in stress (50% lower). Also, the improvement in electrochemical and mechanical characteristics by the second- and third-level pores was confirmed through the development of an electro-chemo-mechanical model on a microelectrode scale. The modeling revealed a gradient in the lithium concentration in both active material and electrolyte of ice-templated-BC, whereas a uniform lithium concentration in ice-templated-SP, which is the main reason for the improved rate capability in ice-templated-SP. In summary, for the first time, we integrated two scalable fabrication technologies to produce tree-inspired hierarchical multiscale porous thick electrodes. These electrodes demonstrate high energy density, outstanding capacity at high current densities, robust structural integrity, and excellent long-term stability, which addresses some current industry challenges regarding thick electrodes and is anticipated to be widely adopted in the practical implementation of manufacturing fast-charging electrodes. Furthermore, given that these three levels of pores created by this route are easily controllable, a comprehensive examination of the correlation between structural, mechanical, and electrochemical properties of electrodes, along with their structural optimization, might be conducted in the future.

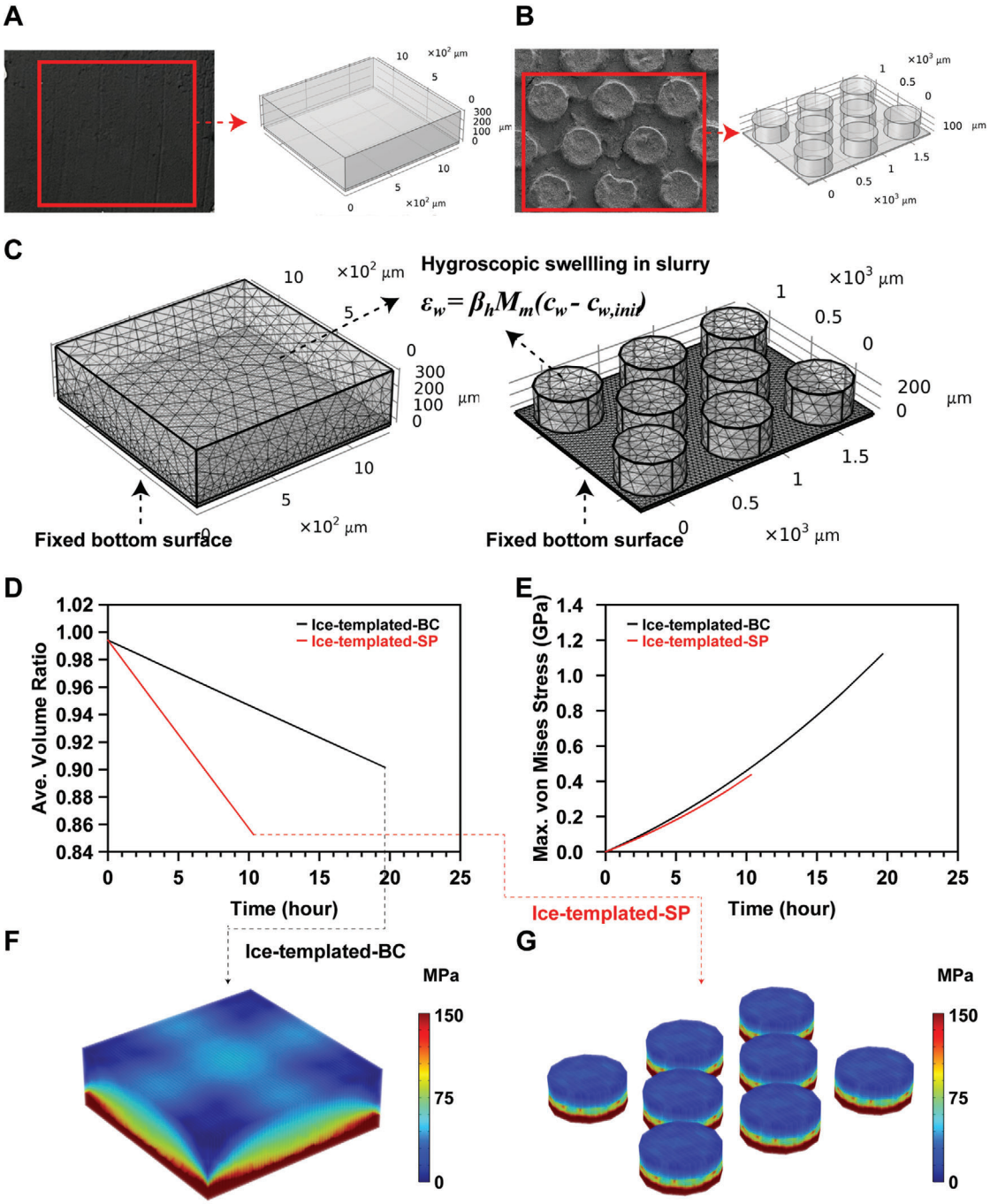


**Figure 6.** Modeling the development of drying and first-level pores effect on mechanical stability. Structure generation for A) ice-templated-BC sample, and B) ice-templated-SP sample. C) Their corresponding meshes, domains, boundaries, and equations along with simulation data: D) volume ratio, E) maximum von Mises stress, and 3D analysis of F) the fully dried ice-templated-BC sample, and G) ice-templated-SP sample.

## 4. Experimental Section

*Materials*: 2,2,6,6-tetramethylpiperidine-1-oxyl (TEMPO), Sodium hypochlorite solution (NaClO solution), sodium bromide (NaBr), microcrystalline cellulose, sodium hydroxide (NaOH), and 98% sulfuric acid were obtained from Sigma-Aldrich, USA. The single crystalline NMC 811 used in this study was sourced from Easpring Material Technology Co., LTD., China. The multiwall carbon nanotube (CNT) was ordered from Tanfeng, LTD., China. The aluminum foil current collector was procured from MTI Co., USA. Prior to slurry manufacture, NMC 811 and Super P powders underwent a drying process in a vacuum oven (MTI Co., USA) for a minimum of 12 h at a temperature of 100 °C.

*Slurry Preparation*: Based on our previous work, the binder consists of acid-included cellulose nanocrystalline ($H^+$ CNC) and cellulose nanofiber (CNF), where the mass ratio of H+ CNC to CNF is 1:1. The synthesis of

CNC and CNF was consistent with our previous publications.[29,30] Briefly, CNC was fabricated by hydrolysis microcrystalline cellulose with concentrated sulfuric acid at 45 °C for 40 min; and CNF was prepared by TEMPO-mediated oxidation using TEMPO, NaBr, NaClO, and NaOH. Before application, the hybrid cellulose binder was well mixed to avoid precipitation and aggregation. The NMC 811, CNT, and binder were added with a weight ratio of 87:10:3 in deionized water to prepare a homogeneous slurry with a solid content of 50%.

*Electrode Fabrication*: The slurry was transferred onto aluminum foil using doctor blade or screen printing techniques. The normal-dried-BC and normal-dried-SP electrodes were dried at ambient temperature. For ice-templated samples, both coated and screen-printed electrodes were positioned on a copper plate that was immersed in a bath of liquid nitrogen. The frozen samples underwent lyophilization (Labconco, USA) at a low temperature of -43 °C. This process was carried out to totally eliminate the water content and produce ice-templated-BC and ice-templated-SP electrodes. Following that, the electrodes were next subjected to a minimum of 4 h at 100 °C in a vacuum oven (MTI Co., USA) before being transferred into the glove box. The porosity of conventional normal-dried-BC electrodes is 45% and that of ice-templated-BC electrodes is 68%. The porosities of ice-templated-SP electrodes are 78% and 54% with and without the first-level pores, respectively. The porosity of electrodes was calculated following equation:

$$\varepsilon_p = 1 - \frac{m_{areal}}{L}\left(\frac{w_{Active\ Material}}{\rho_{Active\ Material}} + \frac{w_{Binder}}{\rho_{Binder}} + \frac{w_{Carbon}}{\rho_{Carbon}}\right) \quad (1)$$

in which the $m_{areal}$, $L$, $p$, and $w$ are the areal mass loading, the electrode thickness, density of materials, and mass fractions of materials.

*Characterization*: The electrolyte utilized in all electrochemical experiments consisted of a solution of 1.2 M $LiPF_6$ dissolved in EC: EMC at a weight ratio of 3:7 (Gen 2). During the construction cell assembly, a volume of 80 µL of electrolyte was applied. Li metal with a thickness of 110 µm was applied as an anode. The Biologic SP150 was utilized to assess the EIS test within the frequency range of 1 MHz to 100 mHz. The galvanostatic testing was conducted using the LANDT 8-channel tester (Wuhan LAND Electronic Co., Ltd). The rate performance and cycling performance were assessed by employing the constant current-constant voltage (CC-CV) charging method at a rate of C/3, as well as by conducting CC discharging ranging from 0.1 to 6C. The electrochemical tests were conducted at ambient temperature. The morphology of the samples was examined using a Hitachi S4800 scanning electron microscope operating at 3 kV. All tests were done at 25 °C.

*Microstructure Reconstruction*: A transfer learning-based approach.[31] is employed to reconstruct 3D stochastic microstructures that are statistically equivalent to given 2D exemplars (Figure S8). This approach utilizes a pre-trained deep convolutional neural network (CNN), e.g., VGG19, to extract microstructure feature map $\boldsymbol{F}$ from 2D exemplars $\boldsymbol{y}$ and iteratively refines the 3D microstructure reconstruction image $\boldsymbol{x}$ in order to fully match the feature map $\boldsymbol{F}$, casting the reconstruction task as an optimization problem. The 3D microstructure reconstruction $\boldsymbol{x}$ is initialized as a random image for the optimization process. This method converts one dimensionality of the 3D image into the batch size, allowing for the comparison of statistical equivalence between 2D segments of the 3D microstructure reconstruction and the reference 2D exemplars. In addition, a permutation operator is employed to ensure the 2D features of the 3D reconstruction across all three directions maintaining statistical equivalency and continuity between adjacent layers. The adoption of the transfer learning approach is motivated by its capability of generating varied types of microstructures and its adaptability to accommodate various formats of reference images, including binary, grayscale, and RGB formats.

The loss function of this approach is defined as the weighted sum of style loss and total variation (TV) loss, which can be expressed as

$$L(\boldsymbol{x}, \boldsymbol{y}) = L_{Style}(\boldsymbol{x}, \boldsymbol{y}) + \alpha L_{TV}(\boldsymbol{x}) \quad (2)$$

$L_{Style}$, style loss, is inspired by the neuron style transfer.[32,33] This term measures the correlations among distinct features within 2D exemplars and the reconstructions across multiple layers of the CNN, typically represented through the Gram matrix. The style loss at layer $l$ can be written as

$$L^l_{style} = \frac{1}{N_l^2 M_l^2}\sum_{i=1}^{N_l}\sum_{j=1}^{M_l}\left(G^l_{ij} - A^l_{ij}\right)^2 \quad (3)$$

where $N_l$ denotes the number of feature maps at layer $l$, $M_l$ denotes the size of feature maps. Here, the Gram matrix $\boldsymbol{G}$ at layer $l$ is computed by

$$G^l_{ij} = \sum_{k=1}^{M_l} F^l_{ik} F^l_{jk} \quad (4)$$

where $\boldsymbol{F}$ represent the reconstruction feature maps captured by the pre-trained VGG model, and, similarly, $\boldsymbol{A}$ represent gram matrix computed by the 2D exemplars features.

$L_{TV}$, total variance loss, is a regularization term used to reduce the high frequency noise produced in the iterative optimization process, which can be acquired as

$$L_{TV}(\boldsymbol{x}) = \sum_{i,j,k}\sqrt{\left(x_{i,j,k} - x_{i+1,j,k}\right)^2 + \left(x_{i,j,k} - x_{i,j+1,k}\right)^2 + \left(x_{i,j,k} - x_{i,j,k+1}\right)^2} \quad (5)$$

The weight factor $\alpha$ of the TV loss term is tuned to ensure a proper balance between the preserving topological features and achieving smooth transitions in greyscale values.

Prior to the reconstruction process, a greyscale image segment with a resolution of 500 nm per pixel and a dimension of 30 × 30 µm$^2$ was extracted from the original SEM image. With a porosity of 45%, the greyscale image is binarized and the binary image is employed as the reference. A 60 × 60 × 60 voxels reconstruction, equivalent to 30 × 30 × 30 µm$^3$, is reconstructed using the proposed approach. The final step, post-processing, includes binarizing the reconstructed image, removing the disconnected solid phase voxels, and fine-tuning the reconstruction to precisely match the target porosity 45%.

Validation of the microstructure reconstruction is conducted by comparing the 2D segments from the 3D reconstruction with the original 2D images, a well-established practice in 2D-to-3D reconstruction problems.[34,35] The 2-point correlation function.[36] is selected as the metric for assessing the statistical equivalence of microstructural features, including dispersion/agglomeration,[37,38] surface area per unit volume,[39] etc. The definition of 2-point correlation function for a binary microstructure image and the validation results are shown in Figure S9 (Supporting Information). The black curves represent the 2-point correlation functions of the 2D segments from the 3D reconstruction, and the red curve with star marks is the 2-point correlation function of the 2D reference images. A good match can be observed between the reconstructed image and the reference images.

*Development of Electro-Chemo-Mechanical Model*: We developed a non-porous model to simulate the electro-chemo-mechanical behavior of the normal-dried-BC sample and Ice-templated-SP sample. Because the active materials and pores are created separately and the electrolyte is filled in the pores (Figures S4A,B, Supporting Information), we can use the non-porous model which is more accurate than a porous electrode model. So, we used the active material's own properties rather than effective values, and the equations became simplified but accurate. The used governing equations are mass conservation (Fick's law), charge conservation (Ohm's law), and kinetic reaction (Bulter-Volmer equation) for electrochemical behavior and lithium-induced strain (hygroscopic swelling) for mechanical behavior as shown in Figure S4C (Supporting Information). We utilized the reported lithium-induced strain, $\varepsilon_s$ with state of lithiation, the molar mass ($M_m$), and lithium concentration change ($c_s - c_{s,\,init}$) to reversely derive the lithium-induced strain coefficient, $\beta_L$.

The current input and fixed boundary are set on the bottom side of the electrode, and the lithium metal (zero potential) is set on the upper side of the structures.

For the simulation of mechanical characteristics, the mechanical model includes the dynamic effect. The governing equation is given by linear momentum conservation in Equation 6 as follows:

$$\nabla \cdot \sigma = \rho \ddot{u} \tag{6}$$

where $\sigma$ is the second order stress tensor and $u$ is the displacement field. We define a small strain tensor $\varepsilon_t$ in Equation 7 as follow:

$$\boldsymbol{\varepsilon}_t = \frac{1}{2}\left(\nabla \boldsymbol{u}^T + \nabla \boldsymbol{u}\right) \tag{7}$$

Also, the mechanical constitutive model was used for the relationship between the total strain $\boldsymbol{\varepsilon_t}$ and stress $\boldsymbol{\sigma}$, which includes the elastic strain $\boldsymbol{\varepsilon}_e$, plastic strain $\boldsymbol{\varepsilon}_p$, and hygroscopic strain $\boldsymbol{\varepsilon}_s$ in Equation 8 as follows:

$$\varepsilon_t = \varepsilon_e + \varepsilon_p + \varepsilon_s \tag{8}$$

The active materials show brittle behavior so, we don't consider plastic deformation in active materials. So, Equation 8 can be written as Equation 9 as follows:

$$\varepsilon_t = \varepsilon_e + \varepsilon_s \tag{9}$$

*Development of Drying Process Modeling*: To analyze the geometrical effect on mechanical behaviors during the drying process of the water-based slurry, the drying process model was developed by assuming the constant drying of the slurry. Also, we applied the active material's properties because it is challenging to measure the slurry's mechanical properties which change in real time with water concentration.

We applied hygroscopic theory for the drying process in Equation 10 as follows:

$$\varepsilon_w = \beta_h \, M_m \left(c_w - c_{w,\,init}\right) \tag{10}$$

where the $\varepsilon_w$ is hygroscopic swelling of the water-based slurry, $M_m$ is the molar mass, $(c_w - c_{w,\,init})$ is water concentration change and $\beta_L$ is the hygroscopic swelling coefficient.

The mechanical behavior during the drying process of the water-based slurry is also simulated based on Equation 6–9.

## Supporting Information

Supporting Information is available from the Wiley Online Library or from the author.

## Acknowledgements

Y.W., J.S., and L.H. contributed equally to this work.This material is based upon work supported by the U.S. Department of Energy's Office of Energy Efficiency and Renewable Energy (EERE) under the Advanced Materials and Manufacturing Technologies Office, Award Number DE-EE0009111. LX and HX acknowledge the financial support from National Science Foundation (CMMI-2142290).

## Conflict of Interest

The authors declare no conflict of interest.

## Data Availability Statement

Research data are not shared.

## Keywords

fast charging, ice-templating, lithium-ion battery, low tortuosity, nickel-rich NMC811, screen printing

Received: July 19, 2024
Revised: September 26, 2024
Published online:

[1] Y. Kuang, C. Chen, D. Kirsch, L. Hu, *Adv. Energy Mater.* **2019**, *9*, 1901457.
[2] D. Cao, Y. Zhao, X. Sun, A. Natan, Y. Wang, P. Xiang, W. Wang, H. Zhu, *ACS Energy Lett.* **2020**, *5*, 3468.
[3] N. Ogihara, S. Kawauchi, C. Okuda, Y. Itou, Y. Takeuchi, Y. Ukyo, *J. Electrochem. Soc.* **2012**, *159*, A1034.
[4] H. Gao, Q. Wu, Y. Hu, J. P. Zheng, K. Amine, Z. Chen, *J. Phys. Chem. Lett.* **2018**, *9*, 5100.
[5] J. Haverkort, *Electrochim. Acta* **2019**, *295*, 846.
[6] H. Ren, Y. Wang, D. Cao, W. Gedney, T. Ji, X. Sun, H. Zhu, *Energy Environ. Mater.* **2023**, *6*, e12584.
[7] H. Ren, E. S. Takeuchi, A. C. Marschilok, K. J. Takeuchi, E. Reichmanis, *Chem. Commun.* **2024**, *60*, 1979.
[8] Z. Du, K. Rollag, J. Li, S. J. An, M. Wood, Y. Sheng, P. Mukherjee, C. Daniel, D. Wood Iii, *J. Power Sources* **2017**, *354*, 200.
[9] K. Rollag, D. Juarez-Robles, Z. Du, I. I. I. Wood, D. L. Mukherjee, P. P. Mukherjee, *ACS Appl. Energy Mater.* **2019**, *2*, 4464
[10] H. R. Brown, *Phys. Perspect.* **2013**, *15*, 320.
[11] L. L. Lu, Y. Y. Lu, Z. J. Xiao, T. W. Zhang, F. Zhou, T. Ma, Y. Ni, H. B. Yao, S. H. Yu, Y. Cui, *Adv. Mater.* **2018**, *30*, 1706745.
[12] Y. Kim, H. Rahardjo, D. L. Tsen-Tieng, *Urban Forestry & Urban Greening* **2020**, *49*, 126639.
[13] Y. Wang, Y. Zhang, D. Cao, T. Ji, H. Ren, G. Wang, Q. Wu, H. Zhu, *Small Methods* **2023**, *7*, 2201344.
[14] Y. Wang, J. He, D. Cao, E. Cakmak, X. Zhao, Q. Wu, Y. Zhao, H. Ren, X. Sun, Y. Li, *Energy Storage Mater.* **2023**, *55*, 42.
[15] D. P. Singh, F. M. Mulder, A. M. Abdelkader, M. Wagemaker, *Adv. Energy Mater.* **2013**, *3*, 572.
[16] R. Xiong, Y. Zhang, Y. Wang, L. Song, M. Li, H. Yang, Z. Huang, D. Li, H. Zhou, *Small Methods* **2021**, *5*, 2100280.
[17] J. Sander, R. M. Erb, L. Li, A. Gurijala, Y.-M. Chiang, *Nat. Energy* **2016**, *1*, 16099.
[18] J. Billaud, F. Bouville, T. Magrini, C. Villevieille, A. R. Studart, *Nat. Energy* **2016**, *1*, 16097.
[19] B. Shi, Y. Shang, Y. Pei, S. Pei, L. Wang, D. Heider, Y. Y. Zhao, C. Zheng, B. Yang, S. Yarlagadda, *Nano Lett.* **2020**, *20*, 5504.
[20] Y. Liu, W. Zhang, Y. Zhu, Y. Luo, Y. Xu, A. Brown, J. N. Culver, C. A. Lundgren, K. Xu, Y. Wang, *Nano Lett.* **2013**, *13*, 293.
[21] X. Xue, D. Lin, Y. Li, *Small Struct.* **2022**, *3*, 2200159.
[22] B. Nie, M. Li, T. Yao, H. Yang, L. Duan, J. Zhang, G. Xin, T. Liu, H. Sun, J. Lian, *CarbonCarbon* **2023**, *206*, 105.
[23] X. Yang, Y. Chen, M. Wang, H. Zhang, X. Li, H. Zhang, *Adv. Funct. Mater.* **2016**, *26*, 8427.
[24] J. S. Yeon, N. Gupta, P. Bhattacharya, H. S. Park, *Adv. Funct. Mater.* **2022**, *32*, 2112509.
[25] Y. Wang, Y. Fang, L. Huang, J. Wang, H. Zhou, G. Wang, Q. Wu, G. Wang, H. Zhu, *Adv. Funct. Mater.* **2024**, 2413865.
[26] J. Song, S. Lim, K. Kim, N. Umirov, H. Lee, C. B. Dzakpasu, J. Lim, J. Nam, J. Park, J. Lee, H. Munakata, K. Kanamura, S. Kim, Y. M. Lee, *Adv. Energy Mater.* **2023**, *13*, 2204328.
[27] J. Song, S. H. Lim, K. G. Kim, N. Umirov, H. Lee, C. B. Dzakpasu, J. Lim, J. Nam, J. Park, J. N. Lee, *Adv. Energy Mater.* **2023**, *13*, 2204328.

[28] J. Park, J. Jeong, Y. Lee, M. Oh, M. H. Ryou, Y. M. Lee, *Adv. Mater. Interfaces* **2016**, *3*, 1600140.
[29] Q. Li, Y. Yin, D. Cao, Y. Wang, P. Luan, X. Sun, W. Liang, H. Zhu, *ACS Nano* **2021**, *15*, 11992.
[30] Y. Wang, A. S. Mijailovic, T. Ji, E. Cakmak, X. Zhao, L. Huang, B. W. Sheldon, H. Zhu, *Energy Storage Mater.* **2024**, *71*, 103546.
[31] R. Bostanabad, *Computer-Aided Design* **2020**, *128*, 102906.
[32] L. A. Gatys, A. S. Ecker, M. Bethge, in Proc. of the IEEE Conf. on Computer Vision and Pattern Recognition, IEEE, Piscataway, NJ, USA **2016**, 2414.
[33] Y. Li, N. Wang, J. Liu, X. Hou, *arXiv* **2017**.arXiv:170101036
[34] H. Xu, D. A. Dikin, C. Burkhart, W. Chen, *Comput. Mater. Sci.* **2014**, *85*, 206.
[35] S. Kench, S. J. Cooper, *Nature Machine Intelligence* **2021**, *3*, 299.
[36] C. Yeong, S. Torquato, *Phys. Rev. E* **1998**, *57*, 495.
[37] H. Xu, Y. Li, C. Brinson, W. Chen, *Journal of Mechanical Design* **2014**, *136*, 051007.
[38] L. Xu, N. Hoffman, Z. Wang, H. Xu, *Mater. Des.* **2022**, *223*, 111223.
[39] Y. Jiao, F. Stillinger, S. Torquato, *Phys. Rev. E* **2007**, *76*, 031110.